

Developing a New Oxygen Atlas of the World's Oceans Using Data Interpolating Variational Analysis

CHRISTOPHER J. ROACH^a AND NATHANIEL L. BINDOFF^{a,b,c,d}

^a *Institute For Marine and Antarctic Studies, Hobart, Tasmania, Australia*

^b *Australian Antarctic Program Partnership, Institute For Marine and Antarctic Studies, Hobart, Tasmania, Australia*

^c *Australian Centre of Excellence in Antarctic Science, Institute For Marine and Antarctic Studies, Hobart, Tasmania, Australia*

^d *Australian Research Council in Climate Extremes, Institute For Marine and Antarctic Studies, Hobart, Tasmania, Australia*

(Manuscript received 8 January 2023, in final form 16 August 2023, accepted 14 September 2023)

ABSTRACT: We present a new global oxygen atlas. This atlas uses all of the available full water column profiles of oxygen, salinity, and temperature available as part of the World Ocean Database released in 2018. Instead of optimal interpolation, we use the Data Interpolating Variational Analysis (DIVA) approach to map the available profiles onto 108 depth levels between the surface and 6800 m, covering more than 99% of ocean volume. This $1/2^\circ \times 1/2^\circ$ atlas covers the period 1955–2018 in 1-yr intervals. The DIVA method has significant benefits over traditional optimal interpolation. It allows the explicit inclusion of advection and boundary constraints, thus offering improvements in the representations of oxygen, salinity, and temperature in regions of strong flow and near coastal boundaries. We demonstrate these benefits of this mapping approach with some examples from this atlas. We can explore the regional and temporal variations of oxygen in the global oceans. Preliminary analyses confirm earlier analyses that the oxygen minimum zone in the eastern Pacific Ocean has expanded and intensified. Oxygen inventory changes between 1970 and 2010 are assessed and compared against prior studies. We find that the full ocean oxygen inventory decreased by $0.84\% \pm 0.42\%$. For this period, temperature-driven solubility changes explain about 21% of the oxygen decline over the full water column; in the upper 100 m, solubility changes can explain all of the oxygen decrease; for the 100–600 m depth range, it can explain only 29%, 19% between 600 and 1000 m, and just 11% in the deep ocean.

SIGNIFICANCE STATEMENT: The purpose of this study is to create a new oxygen atlas of the world's oceans using a technique that better represents the effects of ocean currents and topographic boundaries, and to investigate how oxygen in the ocean has changed over recent decades. We find the total quantity of oxygen in the world's oceans has decreased by 0.84% since 1970, similar to previous studies. We also examine how much of this change can be explained by changes in water temperature; we find that this can explain all the changes in the upper 100 m but only 21% of the oxygen decline over the whole water column.

KEYWORDS: Ocean; Ship observations; Variational analysis; Interdecadal variability; Climate change; Marine chemistry

1. Introduction

Ocean oxygen concentration in the near-surface regime is controlled by a combination of oxygen production during photosynthesis, solubility, and air–sea gas exchange, while at deeper levels oxygen consumption by respiration and redistribution by a combination of circulation and mixing are the dominant factors. Both regional (e.g., Whitney et al. 2007; Sasano et al. 2015; Bograd et al. 2015) and global studies (e.g., Helm et al. 2011; Ito et al. 2017; Schmidtko et al. 2017; Ito 2022) have identified a decline in oxygen concentration across much of the world's oceans. The IPCC Special Report on the Ocean and Cryosphere in a Changing Climate (SROCC) (Bindoff et al. 2022) concluded that “there is a growing consensus that the open ocean is losing oxygen overall with a very likely loss of 0.5%–3.3% between 1970 and 2010 from the ocean surface to 1000 m.” This oxygen loss is also associated with an “unabated warming” and that it is “likely that the rate

of ocean warming has increased since 1993” and that it is “very likely that the upper ocean is stratifying” and “that nutrient cycles have been perturbed (high confidence)”.

By combining the available estimates of oxygen loss from the literature SROCC (Bindoff et al. 2022) assessed, it was very likely the global oxygen inventory had declined by 0.2%–2.1% in the upper 100 m and by 0.7%–3.5% between 100 and 600 m. The decline in oxygen content is negatively correlated with ocean heat content (Ito et al. 2017), and studies suggest that between 15% and 50% (Bindoff et al. 2022) of the oxygen decline in the upper 1000 m can be explained by solubility changes driven by ocean warming. The role of changes in ocean stratification, ventilation, and respiration are more difficult to assess (Oschlies et al. 2018) but likely act to reinforce the warming signal.

Oxygen is an important ocean state variable and is the third most common measured variable after temperature and salinity. The sampling methods used to collect dissolved oxygen data are well established over the observational period (e.g., Montgomery et al. 1964; Gamo and Horibe 1980; Culbertson 1991; Dickson 1994; Langdon 2010). Since oxygen observations

Corresponding author: Christopher J. Roach, christopher.roach@utas.edu.au

are sparse and scattered in both space and time, to properly assess how ocean oxygen content has changed on decadal time scales it is necessary to construct gridded atlases. Historically, most gridded atlases were created using optimal interpolation (OI) or similar approaches in which a prescribed covariance function is used to determine the influence of data on a grid point while seeking to minimize the error variance. However, the covariance functions used are usually simple in nature and often not constrained by ocean physics which can lead to a range of issues including the “leakage” of signals between seas separated by narrow regions of land, the mixing of water masses leading to artificial water masses (Lozier et al. 1994), or the loss of fronts. More recently numerical models combined with data assimilation techniques have been used to produce time-evolving fields of state variables, for example, SODA (Carton and Giese 2008) and ECCO (Wunsch et al. 2009). Applying such methods to oxygen data or other biogeochemically active tracers requires coupling with biogeochemical models. While this approach was implemented in several studies, such as B-SOSE (Verdy and Mazloff 2017), it remains computationally expensive, implying compromises in resolution or domain size. Further, there are significant biases from the uncertainty in the parameters in the biogeochemical models (Buchanan et al. 2018) forcing significant trade-offs and potential biases in the state estimates of temperature, salinity, oxygen, and nutrients.

Ideally, we would like to combine the relative computational efficiency of OI with the realistic physical constraints of numerical models while also avoiding biases in the parameterizations in biogeochemical models (Buchanan et al. 2018) and full state estimation as used in adjoint models. This was achieved through a hybrid approach, using variational inverse methods (VIM), that includes advection of tracer but avoids the complexity of a full biogeochemical model. Variational inverse methods differ from OI in that instead of seeking to minimize error variance VIM seeks to minimize a cost function which includes, at a minimum, terms for closeness of fit to observations and field smoothness (Troupin et al. 2012). VIM based methodologies have been implemented by Troupin et al. (2012) as the Data Interpolating Variational Analysis (DIVA) package in Fortran, which supports 2D analysis on finite element grids and by Barth et al. (2014) as the DIVAnd package (<https://github.com/gher-ulg/DIVAnd.jl>) in Julia, which supports 3D and 4D analyses on curvilinear grids. Data Interpolating Variational Analysis has previously been applied on regional scales to generate temperature and salinity climatology for the North Atlantic (Troupin et al. 2010), map mixed layer and cold layer depths in the Black Sea (Capet et al. 2014), create climatologies of inorganic nutrients in the Mediterranean Sea (Belgacem et al. 2021), and to produce gridded sea surface height in the Arctic (Dogliani et al. 2023).

In this study we use DIVAnd (Barth et al. 2014) to produce a new atlas of oxygen concentration, conservative temperature, and absolute salinity. We have taken into account time as well, thus making the atlas suitable for climate change studies of the oceans changing state on scales of about a decade up to 50 years. This atlas comes as new oxygen-sampling floats that were tested during the SOCCOM experiment (Riser et al.

2018) are being expanded to form the basis of a global network (Claustre et al. 2020). This global atlas (80°S–80°N) has been created on a $1/2^\circ \times 1/2^\circ$ grid on 108 depth levels with a temporal resolution of 1 year. Effective resolution on local scales varies on the data and VIM constraints.

In section 2 we describe the datasets used in this study. In section 3 we describe our methodology including the DIVAnd fitting procedure, how we selected DIVAnd parameters, and the error analysis. In section 4 we present our results and in section 5 we conclude the work and discuss its merits relative to past approaches and potential application.

2. Data

a. World Ocean Database

The World Ocean Database (WOD) is a repository of standardized and quality controlled oceanographic profiles maintained by NOAA, containing data from the earliest days of oceanography up until the present. WOD was first released in 2005, and has been regularly updated since, with the most recent major release occurring in 2018 (hereafter referred to as WOD18). Details of WOD18 processing and quality control can be found in Boyer et al. (2018) and Garcia et al. (2018). WOD18 interpolates profiles to 137 depth level between the surface and 9000 m depth. However, below 6100 m (depth level 108) there is very little ocean volume (e.g., at 6100 m depth ocean grid cells make up only 0.3% of the domain); hence, we exclude these deeper depth levels from this study.

While the WOD18 archive includes data from BioArgo and SOCCOM floats, calibration techniques to counter sensor drift were not fully developed and deployed until late in the database’s coverage (Bittig and Körtzinger 2015; Bushinsky et al. 2016); thus, we exclude float data from this study and focus on shipboard profiles of oxygen, temperature, and salinity. Profile data from ships tend to be higher quality and in the experience of these authors tend not to include difficult to manage biases and quality characteristics found in sensors from float and expendable measurements (e.g., XBTs). As seen in Figs. 1b and 1c, shipboard observations are sparse in the Southern Hemisphere and at depth levels below about 4000 m prior to the late 1950s; hence, we confine our analysis to the period between 1955 and 2018. We then opted to only use the higher quality data (that is, data flagged as 0, “all good”) in WOD18 data files. Additionally for each depth level we computed the background, or, a priori error variance of the data as (Wong et al. 2001)

$$\sigma_{\text{apriori}}^2 = \sum_{i=1}^n (d_i - d_j)^2 / 2n,$$

where d_i and d_j are a pair of closely spaced observations (here, less than 1° apart in both longitude and latitude), and n is the total number of observations on the depth level. This estimate of a priori noise represents the unresolved ocean processes in the observations at scale of order 1° – 2° and included mesoscale eddies, internal waves, and other ocean variability. Pairs of nearest-spaced data with differences exceeding the $\pm 2\sigma_{\text{apriori}}$ range were excluded from this analysis as these

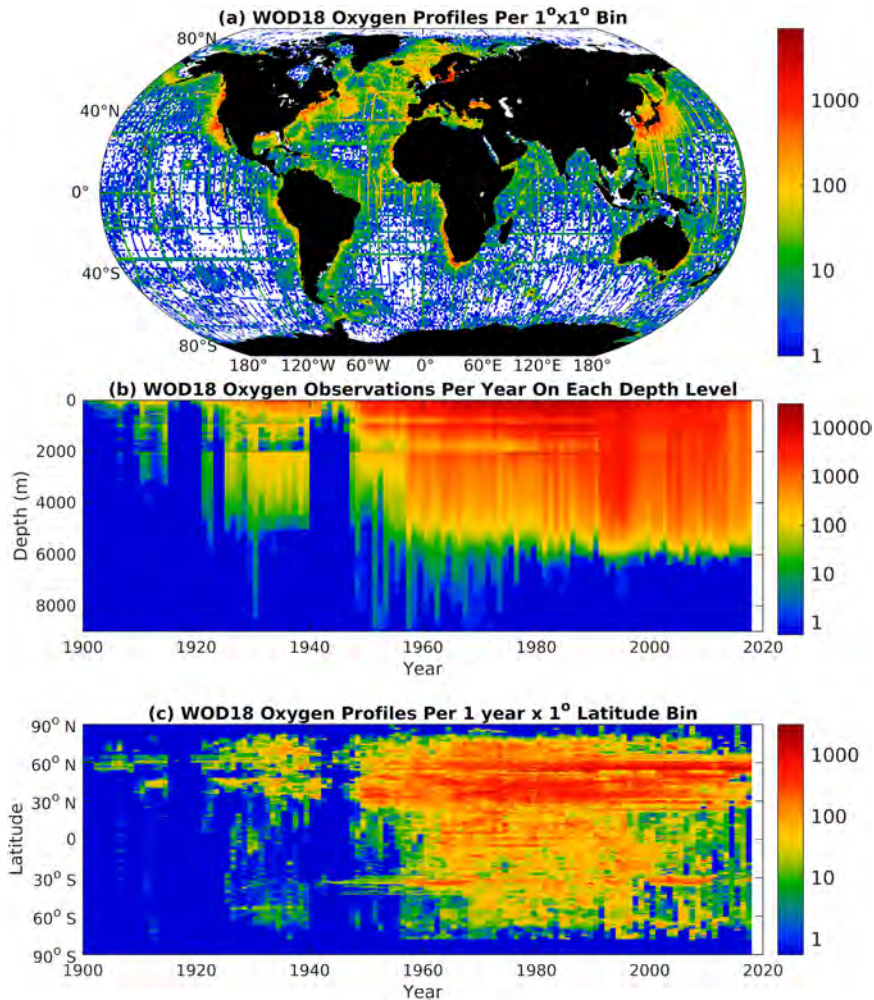


FIG. 1. Distribution of shipboard oxygen profiles from the World Ocean Database 2018. (a) The spatial distribution (profiles per $1^\circ \times 1^\circ$ bin) emphasizes coastal regions and repeat ship surveys. The distributions by (b) depth and time and (c) depth and latitude show the scarcity of profiles below about 4000 m and south of 30°N before the late 1950s.

data likely represent a combination of small-scale or high-frequency features we are unable to resolve in this analysis and erroneous data.

Having applied this QC process, we obtained a total of 818 484 oxygen profiles (out of 1 138 226), 2 194 406 temperature profiles (out of 3 986 254), and 2 758 094 salinity (out of 3 488 851) profiles for the period up to 2018. Temperature and salinity were converted to conservative temperature and absolute salinity using the GSW MATLAB toolbox (McDougall and Barker 2011).

Our choice of shipboard data does impose a seasonal sampling bias at high latitudes, with sampling in the Arctic (above about 75°N) and Antarctic margins (below about 60°S) mostly concentrated in the summer months. This pattern of sampling bias remains robust throughout the period of the experiment, and as such is unlikely to contribute to long-term oxygen trends.

b. CMCC historical reanalysis velocity fields

In this study we use velocity fields from the CMCC Historical Ocean Reanalysis (Yang et al. 2017), RL version (<http://c-glors.cmcc.it/index/index-3.html?sec=2>), as the advection constraint in the DIVAnd analysis. The CMCC Historical Ocean Reanalysis (CHORS) products used the NEMO ocean model in the ORCA05 configuration, forced with atmospheric and solar forcing from the Twentieth-Century Reanalysis version 2 (Compo et al. 2006). Hydrographic profiles, principally from the Hadley Center “EN” collection, were assimilated into the model using a 3D-Var approach (Storto et al. 2011) while sea surface temperature was relaxed to the Hadley Centre’s Sea Ice and Sea Surface Temperature dataset (Rayner et al. 2003).

Studies of climate change in CMIP5 models suggest that large-scale ocean circulation is only weakly sensitive to climate change (Terada and Minobe 2018). Thus, the temporal variation of the velocity field is assumed to be small and we

use CHORS reanalysis zonal and meridional velocity fields averaged over the period 1960–2016. This use of a time-mean velocity fields means that our atlas is unable to resolve any currents that evolve on a seasonal time scale (e.g., monsoon surface current in the northern Indian Ocean).

3. Methods

a. Data Interpolating Variational Analysis

Data Interpolating Variational Analysis (Troupin et al. 2010; Barth et al. 2014) is a mapping or interpolation method which seeks to find an optimal tracer field for given observations by minimizing a cost function which includes terms for field smoothness and the residual between the tracer and observations and, optionally, terms for further constraints including the influence of advection and boundary conditions arising from topography. Details of implementation of DIVAnd can be found in Barth et al. (2014). Example application of Data Interpolating Variational Analysis to both realistic and idealized scenarios can be found in Barth et al. (2014), Troupin et al. (2012, 2017), and at <https://github.com/gher-uliege/Diva-Workshops>.

The “core” constraints consist of two terms, an observation constraint which penalizes data-analysis misfit $[d_j - \phi(x_j)]^2$ and a smoothness constraint which penalizes field curvature $\|\phi - \phi_b\|^2$:

$$J(\phi) = \sum_{j=1}^n \mu_j [d_j - \phi(x_j)]^2 + \|\phi - \phi_b\|^2 + J_c(\phi), \quad (1)$$

where d_j are the observations at locations x_j with a weighting μ_j , ϕ is the analysis tracer field, ϕ_b is the background field, and $\|\cdot\|$ denotes the L2 norm.

Equation (1) can be reexpressed as Belgacem et al. (2021):

$$J(\phi) = \sum_{j=1}^n \mu_j L_c^2 [d_j - \phi(x_j, y_j, t_j)]^2 + \int_D (a_2 \nabla \nabla_\phi : \nabla \nabla_\phi + a_1 L_c^2 \nabla_\phi \cdot \nabla_\phi + a_0 L_c^4 \phi^2) dD + J_c(\phi), \quad (2)$$

where L_c is the correlation length scale (usually defined in the zonal, meridional, and time directions L_x , L_y , and L_t); the coefficients a_0 (minimizing field anomalies), a_1 (minimizing spatial gradients), and a_2 (penalizing field variability) are set internally by the DIVAnd program; ∇_ϕ is the gradient of the tracer field, $\nabla \nabla_\phi : \nabla \nabla_\phi$ is the squared Laplacian of the tracer field; μ_j is an arbitrary weighting applied to the data to reflect considerations such as data quality (in this study we apply a uniform weighting to all data as all “bad data” have been excluded); and $\int_D \cdot \cdot \cdot dD$ denotes the integral across the domain.

Additional constraints $[J_c(\phi)]$ can be included, in this study we used the advection constraint $[J_a(\phi, \mathbf{U})]$ and coastal boundary constraint built into DIVAnd. The coastal boundary constraint penalizes nonzero near-coast tracer field gradients. The advection constraint penalizes any misalignment between the analysis tracer field and a specified vector field:

$$J_a(\phi) = w_u^2 \int_D (\mathbf{U} \cdot \nabla_\phi)^2 dD,$$

where w_u is the advection weighting, \mathbf{U} is the vector field (usually velocity), and \cdot denotes the dot product.

When the gradient of the tracer field is close to perpendicular to the vector field $\mathbf{U} \cdot \nabla$ is small and the penalty imposed by the cost function is, thus, low, as the gradient of the tracer field aligns more closely with the vector field this term becomes larger and the penalty imposed increases.

The cost function can then be expressed as a matrix equation [see Barth et al. (2014) for details] which can then be solved by factorization using the CHOLMOD factorization package (Chen et al. 2008; Davis and Hager 2009).

b. DIVAnd fitting procedure

We assume that on each depth level the field F_{tot} of a given tracer can be decomposed into three terms:

$$F_{\text{tot}} = F_y(y) + F_{\text{BG}}(x, y) + F_t(x, y, t);$$

F_y represents the zonal-mean dependency of a tracer on latitude. This is estimated by applying a low-order polynomial fit to all data on a given depth level. This is necessary as otherwise areas with few data relax back to the global mean value. The second term on the right-hand side, F_{BG} , is the time-mean background tracer anomaly field from the latitude-dependent mean F_y and F_t is the time-varying tracer anomaly.

We convert the observational data into anomalies relative to F_y (i.e., $F_{\text{obs}} - F_y$), then run a 2D (longitude–latitude) DIVAnd analysis to obtain F_{BG} , then reanomalize the observations as $F_{\text{obs}} - (F_y + F_{\text{BG}})$, and then run a 3D (longitude–latitude–time) analysis to obtain F_t . Due to computational resource constraints this final step is implemented by solving F_t for series of overlapping 10-yr windows. This mapping procedure is applied to oxygen, conservative temperature, and absolute salinity data on all 108 depth levels between 0 and 6100 m. The temporal extent of the interpolation runs from 1955 to 2020 at 1-yr intervals (notionally 1 January of each year), but due to boundary effects and availability of data only the years 1960–2017 are included in the published atlas.

c. Selecting parameters

The DIVAnd fit, described above, depends on a set of correlation scales, an advection weighting, and the signal-to-noise ratio. As the time-mean DIVAnd fit is followed by a time-varying fit we opt to moderately underfit and thus consider signal-to-noise ratios between 1.15 and 1.2. For $L_x = 500$ km this suggests an advection weighting of 1 is acceptable. We describe how these correlations scales and advection weightings are selected. Conventionally, one would use an iterative application of generalized cross validation (GCV) to select optimal decay scales, advection weightings and signal-to-noise ratio. However, in this case GCV is impractical. Shipboard observations are generally clustered in time and space along ship tracks. As a consequence of this distribution of measurements the application of GCV produces unrealistically high signal-to-noise ratios and short correlation scales (Troupin et al. 2012). Instead for each depth level we estimate univariate covariance functions in longitude, latitude, and time based on a random subsample of observations. This reduces the sampling effects from long

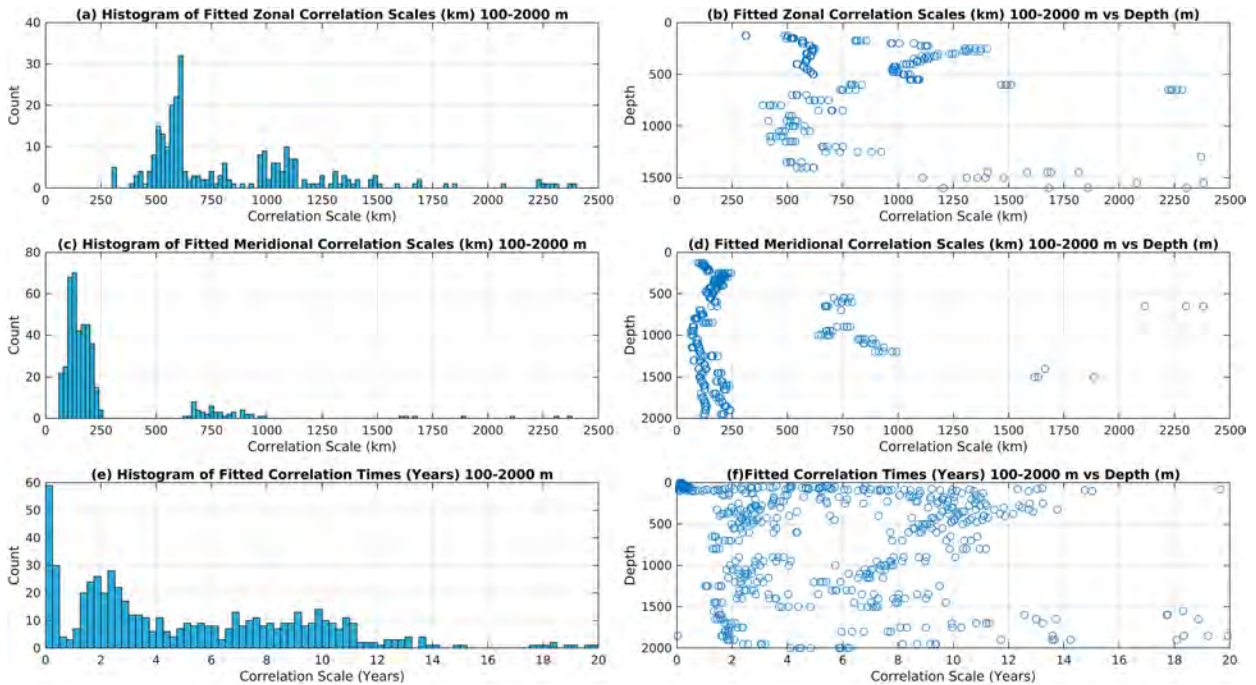


FIG. 2. (a),(c),(e) Histograms of fitted correlations scales and (b),(d),(f) scatterplots of correlation scales as a function of depth.

hydrographic lines. We then assume the covariance function can be represented as either

$$C = sK(L) + C_{\text{off}} \quad (3a)$$

or

$$C = sK(L), \quad (3b)$$

where K denotes the DIVAnd kernel, L the decay scale, s is a scale factor, and C_{off} a correction for any large-scale “background” covariance.

We then fit Eqs. (3a) and (3b) to the covariance estimate using least squares optimization. Estimation of the covariance and the fits are repeated 50 times, giving us a total of 100 estimates for L_x , L_y , and L_t on each depth level.

Scatterplots and histograms of correlation scales are shown in Fig. 2. Examination of temporal covariance shows strong seasonal-scale signals in the upper 100 m, while estimates of temporal covariance range from seasonal time scales within the upper 100 m, likely also accounting for the exceptionally long zonal correlation scales observed at the surface, to 8–12 years below 200 m. At depths over 2000 m, the observations are insufficient for reliable fits to these equations. This analysis suggests that the most suitable choice (dictated by a peak in the correlation-scale histograms) of zonal correlation scale is about 500 km and meridional correlation scale is about 100 km and 2.5 years for correlation time. However, the presence of mesoscale features and the heterogeneous nature of the sampling, in both time and space, from along a single cruise track (generally less than 200 km in distance, and hours to days in time) compared with the spacing of observations from many different cruises

(500 km or more in space and months to years in time) implies that these correlation scales could still be biased low. The zonal correlation scale is already sufficiently large that this is unlikely to be an issue. However, as a precaution we opted to increase the meridional correlation scale to 250 km.

Interpolation of any form represents a trade-off between the ability to recreate data at observations (low residuals) and field smoothness while not overfitting or underfitting (i.e., obtaining a signal-to-noise ratio close to 1). Hence, to determine an appropriate choice of advection weighting and validate our choice of decay scales, we produced time-mean DIVAnd fits at 500 m depth for a range of different L_x and w_u , with L_y fixed as $L_x/2$ from which we computed and plotted signal-to-noise ratios (defined here as $\sigma_{\text{signal}}^2/\sigma_{\text{apriori}}^2$) and field roughness (here, the variance of the horizontal oxygen gradient, or salinity or temperature gradients). These results are shown in Figs. 3a and 3b, respectively.

Our desired signal-to-noise ratio (1.15 and 1.2, the white contours shown in Fig. 3) excludes most of the L_x - w_u state space. Choices of shorter decay scales less than about 100 km do not extend the influence of data far enough in space, and thus, areas some distance from ship tracks relax back to the large-scale meridional background estimate. This results in unrealistically rough fields and is indicative of overfitting of the observations (appendix Fig. A1b). Zonal decay scales of around 200–300 km perform better, resulting in a less rough background oxygen concentration map (appendix Fig. A1c), but still retain some unreasonably strong gradients and traces of ship tracks (e.g., the low-latitude North Atlantic, appendix Fig. A2c). Long correlation scales (greater than about 800 km) produce smoother fields (appendix Fig. A1d) but examination

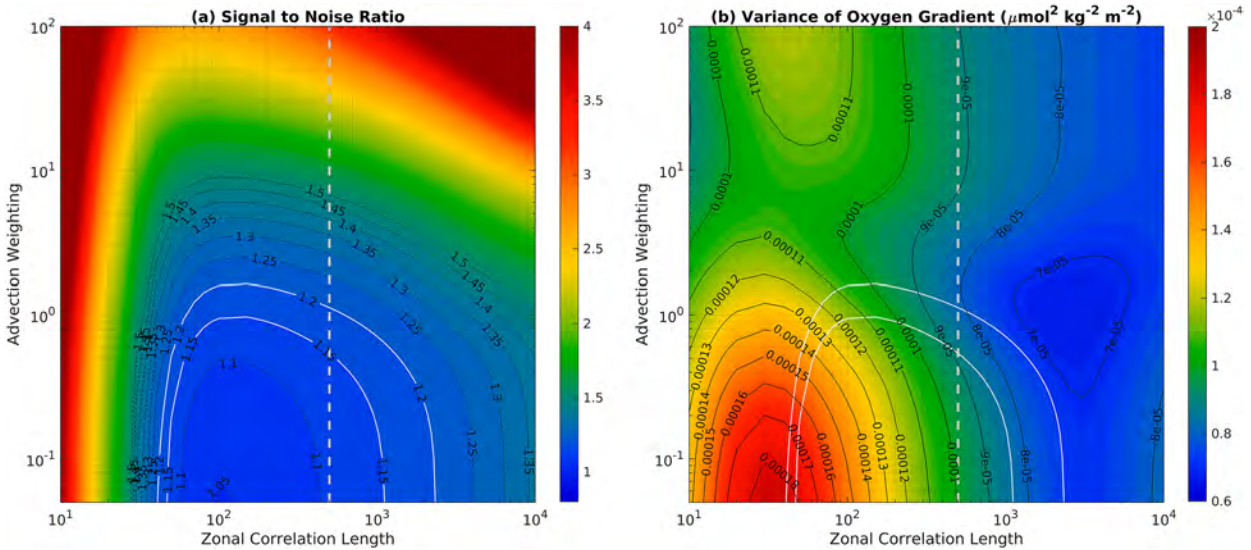


FIG. 3. Background fit (a) signal-to-noise ratio and (b) oxygen gradient variance at 500 m for $L_y = L_x/2$. White contours indicate the target signal-to-noise ratio range and the gray dashed line indicates the selected zonal correlation scale.

of spatial correlations (e.g., appendix Fig. A2d) demonstrate that these long correlation scales erode the ability of the analysis to resolve dynamical barrier in the velocity fields. Tests with $400 < L_x < 600$ km and $w_u \approx 1$ show little difference to our selected parameters of $L_x = 500$ km and $w_u = 1$ (not shown). We are, thus, confident that our choice of correlation scales and advection weighting are close to optimal.

d. Error analysis

Given a covariance matrix \mathbf{C} and data vector \mathbf{g} , errors can be propagated as (Tellinghuisen 2001)

$$\sigma^2 = \mathbf{g}^T \mathbf{C} \mathbf{g}.$$

DIVAnd returns an inverse relative grid–grid covariance matrix (\mathbf{C}^{-1}), where covariance is normalized by the a priori variance; we thus treat \mathbf{g} as a vector of ones, and we can compute as the total variance on each depth level as

$$\sigma^2 = \sigma_{\text{apriori}}^2 \cdot \mathbf{g}^T \mathbf{C} \mathbf{g}. \tag{4}$$

However, as the inverse covariance matrix \mathbf{C}^{-1} is a large, sparse matrix, “brute force” inversion is impractical as inversion produces a large, dense matrix which in turn runs into memory limitations. To avoid it is necessary to obtain an expression in terms of (\mathbf{C}^{-1}). To do this let us consider

$$\mathbf{x} = \mathbf{C} \mathbf{g}.$$

Multiply this system through by \mathbf{C}^{-1} :

$$\mathbf{C}^{-1} \cdot \mathbf{x} = \mathbf{C}^{-1} \cdot \mathbf{C} \mathbf{g},$$

which simplifies to

$$\mathbf{C}^{-1} \cdot \mathbf{x} = \mathbf{g}.$$

Given a known \mathbf{C}^{-1} and \mathbf{g} this system can be solved for \mathbf{x} . Using \mathbf{x} to denote the solution of the above system, the full expression for error propagation [Eq. (4)] becomes

$$\sigma^2 = \sigma_{\text{apriori}}^2 \cdot \mathbf{g}^T (\mathbf{g} \mathbf{C}^{-1}). \tag{5}$$

Computing confidence intervals from standard deviations obtained from Eq. (5) assuming a specific distribution or using Student’s t test requires estimating the effective degrees of freedom. Both approaches to this problem are nontrivial to solve (Janson et al. 2015). Computing error fields using the coefficient of determination (Bretherton et al. 1976), as applied in Ito (2022), requires approximating data–data and data–grid covariance matrices from the grid–grid covariance matrix, which in turn runs into the compute and storage limitations described above. Instead, we used Chebyshev’s inequality (Tchebichef 1867) to obtain a “pessimistic” estimate of confidence intervals. Chebyshev’s inequality states that the probability of a data point (X) lying within k standard deviations of the mean is

$$P(|X - \mu| > k\sigma) < k^{-2}.$$

From this inequality, a $\pm 2\sigma$ range corresponds to a 75% confidence interval, while 95% confidence intervals correspond to a $\pm 4.4721\sigma$ range. We opt to report uncertainty in vertically integrated gridded inventories with the 2σ range and globally integrated inventories with 95% confidence intervals.

4. Results

We have constructed an atlas of the oxygen, salinity, and temperature data from all of the research quality profile data compiled in the 2018 version of the World Ocean Database from the mid-1950s to 2018 (Roach and Bindoff 2023). The

underlying climatology or reference field created for this atlas includes all of the available shipboard data from the 1950s to 2018. Consequently, its precise reference period for the underlying climate is reflected in the time weighted average of the all the data used to create the underlying climatology. Because the data distribution is heterogeneous in time, depth, and geographic location (Figs. 1a–c) its precise time varies by location depending on how the covariance field weights observations, but can generally be thought of as an early to mid-1990s average. This climatology is used to create the anomaly field of oxygen (and temperature and salinity) shown below.

a. Testing the mapping method

Atlases of oceanographic temperature, salinity, and oxygen are a well-established tradition in oceanography (e.g., Wüst 1936; Levitus 1983; Wunsch 1996; Ridgway et al. 2002; Fukumori et al. 2018). A key advantage of the DIVA approach is its capacity to include advection as a specific constraint on the circulation with explicit boundary conditions for coastlines. The inclusion of advection through the tracer equation and the explicit boundary conditions for coastlines largely overcomes two very common problems in mapping of ocean fields using optimal interpolation (Bindoff and Wunsch 1992). The first problem is that optimal interpolation often uses a simple circular or elliptical covariance functions, with advection at most being represented by a stretching or rotating of the ellipse as in Ducet et al. (2000). As a result OI can smooth tracers across dynamical barriers, creating false water masses (Lozier et al. 1994), or suppressing fronts. The second problem is OI does not include any coastal boundary conditions; thus, signals can propagate through land barriers. These problems can force atlases to neglect marginal seas as in Ito (2022) or require complicated regional masking regimes.

DIVAnd's ability to solve these problems is demonstrated in the upper and middle panels of Fig. 4 which show example spatial correlation plots for the 50 m depth level in the year 1975 for grid points in the Kuroshio (32°N, 133°E; left) and eastern Pacific (7.5°N, 83°W; right), which compare correlation for optimal interpolation (Figs. 4a,b) with correlation for DIVAnd (Figs. 4c,d). We see that in both cases DIVAnd propagates correlation along advection pathways while OI does not. This implies that DIVAnd is more realistic in regions of strong flow where observations a long way up- or downstream influence a grid point. We also see that DIVAnd resolves dynamic barriers, as can be seen in proximity to the standing eddy-like structure near 31°N, 133°E in Figs. 4a and 4c. Under this circumstance, OI would behave in an unrealistic manner and include the influence of observations on the wrong side of the dynamical barrier, oversmoothing the CT, SA, and oxygen fields and potentially creating false water masses.

To check that DIVAnd was not creating artificial water masses or oversmoothing fronts, we interpolated the full, time varying temperature, salinity, and oxygen fields back onto the times and places of observations. Example CT–oxygen and SA–CT histograms for the Kuroshio region, selected as a region dominated by fronts with sharp boundaries between water masses, are shown in Figs. 4e and 4f, both demonstrate

good agreement between the DIVAnd analysis and the “raw” WOA18 observations. Similar plots were produced for other regions with strong frontal features and show equally good agreement.

b. Oxygen inventory

The oxygen atlas that has been created has both the underlying mean state through the full water column and also the changes from this mean underlying state. The large-scale mean state of oxygen through the full water column using the available hydrographic data and DIVA is shown in Fig. 5.

The background oxygen concentration at 100 and 500 m is shown in Figs. 5a and 5b. The background fields represents the average of the ocean state of about 1993 after factoring in time density of the hydrographic data. Estimates of errors are available for the underlying field, but these are very small relative to the large-scale variations and consequently have been omitted on these two panels. Overall, the features of the oxygen gradients and content are consistent with our large-scale understanding of the mean oxygen field (e.g., Wüst 1936; Wunsch 1996; Fukumori et al. 2018). Even in this relatively shallow layer the presence of the strong oxygen minimum in the equatorial and subtropical eastern Pacific, northern Indian, and Atlantic Oceans can be seen. The high values in this layer, where mixed layers are thicker the polar regions (south of the Antarctic Circumpolar Current), and the local minima at the Antarctic divergence before increasing again toward the Antarctic coastline. The Arctic also shows high values of oxygen. These high values of oxygen in the polar regions are near saturation (see next section for more detail).

In the equatorial regions, the deeper 500 m layer (Fig. 5b) intersects the main core of the oxygen minimum and cuts through the main thermocline of the subtropical gyres and the mode waters on the equatorward side of the western boundary currents and the Antarctic Circumpolar Current. This figure also shows the extended region of the oxygen minimum waters in the equatorial region. They extend from the eastern Pacific to almost the western side of the Pacific Ocean, extend southward and cross the equator in the Indian Ocean. In the Atlantic sector the oxygen minimum is weaker in value but its signature extends across the whole of this ocean. The subtropical gyres (Northern and Southern Hemispheres) show quite high values consistent with the known ventilation areas (Talley et al. 2016) on the equatorward side of the main western boundary currents in the Northern Hemisphere and the Antarctic Circumpolar Current in the Southern Hemisphere. The circumpolar band of low oxygen in south of the Antarctic Circumpolar Current is the upwelling low oxygen Circumpolar Deep Waters (CDW) (Fig. 5b).

These maps have been created with the mean velocity field and constrained by both the horizontal tracer advection and also the boundary conditions at continental boundaries (section 3). Consequently, the maps show local extrema that might be otherwise smoothed out in optimal interpolation (Lozier et al. 1994) at coastal margins; this is particularly evident in the oxygen minimum layer on the eastern boundaries of the equatorial Pacific

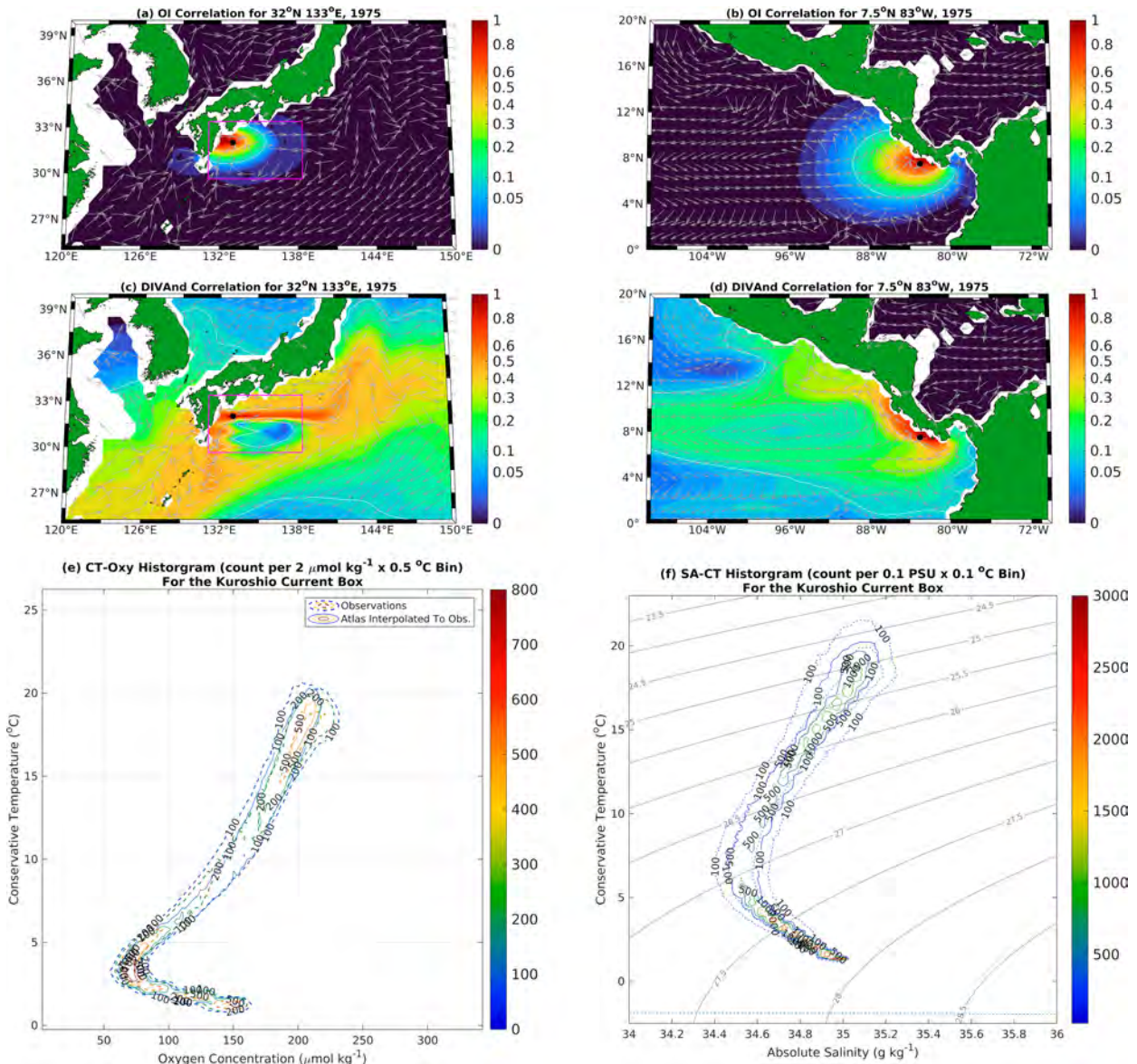


FIG. 4. Example correlation maps (1975; 50 m depth) for optimal interpolation and DIVAnd relative to (a),(c) 32°N, 133°E in the Kuroshio region and (b),(d) 7.5°N, 83°W in the Pacific south of Panama; vectors indicate current heading and the black dot indicates the reference grid point. (e) Conservative temperature–oxygen and (f) conservative temperature–salinity histograms for WOA18 observations (dashed contours) and values interpolated from DIVAnd fields (solid contours) in the region indicated by the pink box in the Kuroshio maps.

and Atlantic Oceans as shown in the 100 and 500 m layers (Figs. 5a,b).

The use of mean flow is also very useful in these maps. For example, the low oxygen signal in the surface waters at the Antarctic divergence also correspond precisely with the point that the eastward surface ocean circulation become eastward (progressing southward). The divergence in the field implying vertical upwelling is not explicitly included in DIVA approach, but the DIVA approach allows the lower oxygen values observed in the data to be preserved as reflected in the map at 100 m (Fig. 5a). Less conspicuous examples in the

figures are the higher oxygen values on the equatorward side of the western boundary currents and Antarctic Circumpolar Current. These (relatively enhanced) oxygen levels also make sense when viewed with the mean flow field, higher near the source regions in the mode waters and gradually declining with the circulation around the subtropical gyres. Further, the sharp boundary between the waters in the oxygen minimum areas near the equator and their distinctive stretched out pattern along the equator, particularly in the Pacific and Atlantic Oceans, can also be more easily understood in terms of the long pathways of these waters, coming around respective

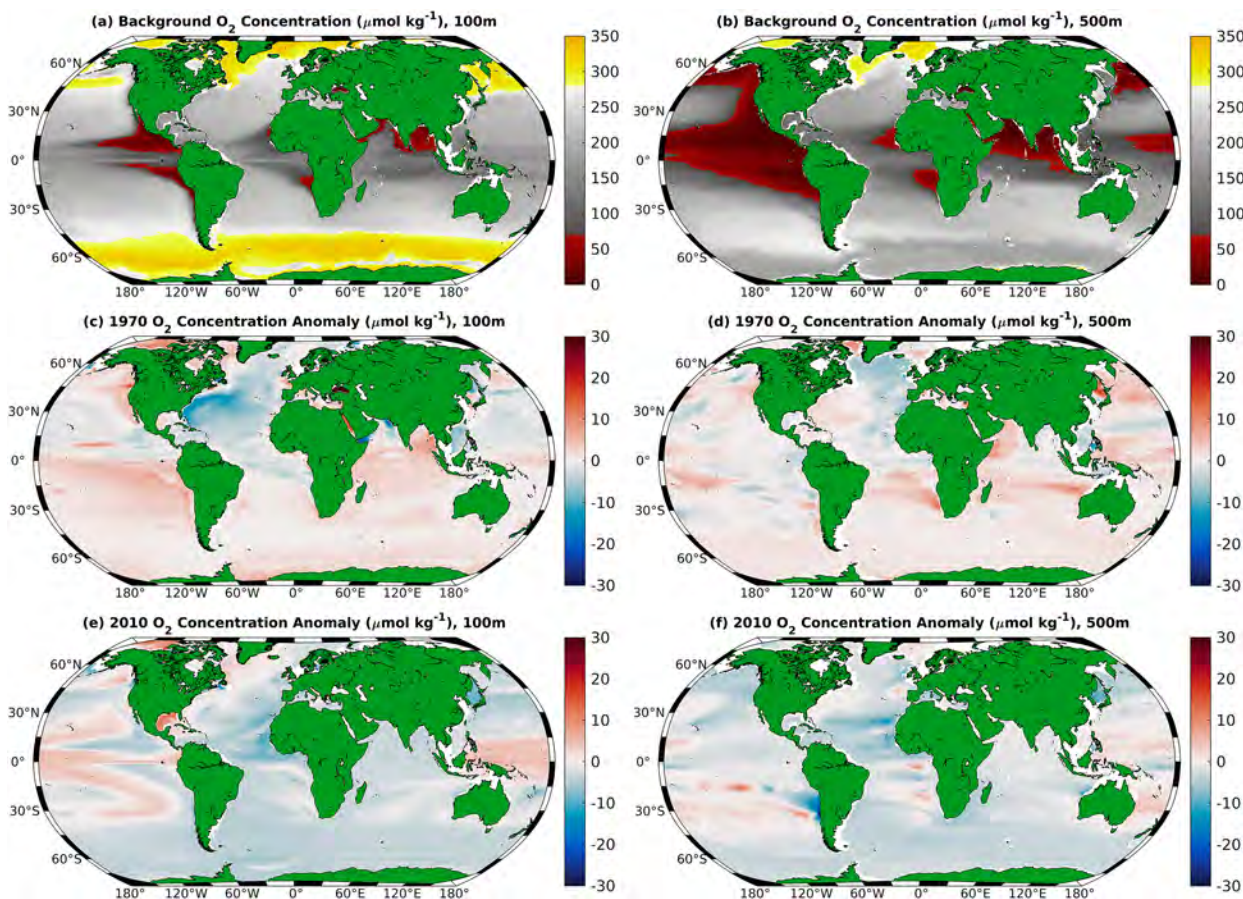


FIG. 5. Maps of (a),(b) background oxygen concentration ($\mu\text{mol kg}^{-1}$) and oxygen concentration anomalies at 100 and 500 m for (c),(d) 1970 and (e),(f) 2010.

Northern and Southern Hemisphere gyres, flowing westward in the near equatorward and then returning eastward along the equator feeding in to the oxygen most oxygen minimum regions in the so-called blind zones (Luyten et al. 1980) (see Figs. 6a,b).

One of the aims of this atlas is to be able to look at the time varying state of oxygen based on the available data, in addition to the steady state. Two examples of the difference of oxygen from the background state are shown for an earlier and later period in the constructed time series. The earlier period of 1970 is before the notional mean date of the background field (early to mid-1990s), whereas the later period of 2010 is after this mean date.

The earlier spatial snapshots (Figs. 5c,d) show for all oceans, except the Atlantic, higher levels of oxygen relative to the background field at both 100 and 500 m depths. The Southern Hemisphere is more distinctive in its pattern of higher oxygen almost everywhere (Fig. 5, middle-left panel). In the equatorial and extratropics the pattern of higher oxygen values tend to mimic the pattern of low oxygen found at this depth and just below. Curiously, the North Atlantic shows lower oxygen concentration relative to the background in 1970, and as explained in the next section this is not explained by simply observed temperature changes.

The spatial snapshots for 2010 (Figs. 5e,f) show a distinctly different pattern (and sign) of oxygen change in the global oceans relative to the background field. At 100 m both hemispheres show a broad decrease in oxygen content in both the Southern, Atlantic, and Indian Oceans. These large-scale changes, which are typically below in the mixed layer (except in formation regions of mode water), are consistent with the previous work that show decline in oxygen relative to the background field. However, there are some distinct regions that show an increase in oxygen below the mixed layer. Particularly in the Pacific Ocean, in a roughly symmetric pattern around the equator, the oxygen levels remain high relative to the background field. This distinct pattern of higher values converge toward the western equatorial warm pool region and this pattern seems nicely tied to the large-scale circulation of the two Pacific gyres (see Fig. 6a). WOCE repeat hydrographic sections in the South Pacific sector show enhanced oxygen in a similar location in the westward flowing part of the South Pacific subtropical gyre (Talley et al. 2016). At depth (e.g., 500 m, Fig. 5f) the oxygen concentration shows higher values than background in these same regions as the 100 m depth level of the Pacific Ocean, but displaced more toward the poles. Overall, the 500 m layer shows a decline, with almost all areas showing negative values with

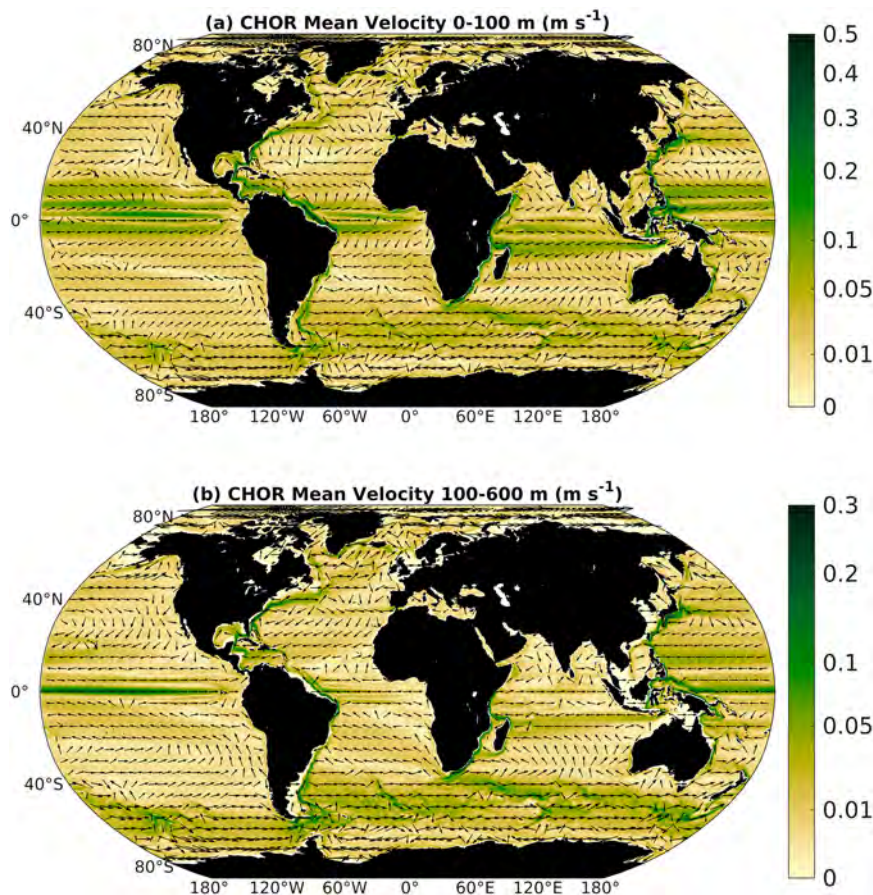


FIG. 6. Maps of mean velocity field used in the DIVA (m s^{-1}) for the (a) 0–100 and (b) 100–600 m layers.

respect to the background field (with exceptions notes above). Relative to the 1970 pattern, the 2010 pattern of change on the 500 m layer is very much a uniform decrease. Indeed, the decrease between 2010 and 1970 seems remarkably uniform.

c. Oxygen inventory changes and drivers of change

Changes in oxygen content are driven by many factors: temperature sets oxygen solubility; biology can act as both a source in the surface waters or a sink in deeper waters; advection can move oxygen rich waters along isopycnals; changes to surface wind fields can drive Ekman-driven upwelling or downwelling of waters; water masses can move vertically within the water column (heave) and changes in stratification can act to enhance or suppress diapycnal mixing. To fully explore all factors lies beyond the scope of this paper.

Time series of oxygen inventory anomalies (relative to the background) for various depth ranges are shown for the period 1970–2010 in Fig. 7. In all depth bands we see a statistically significant decrease in oxygen inventories between the 1970s and 2000s with the decline predominately occurring from the late 1980s onward. The upper ocean (0–100 m), full ocean, and deep ocean (>1000 m) show possible decadal-

scale variability, with peak oxygen inventories occurring in the mid-1980s; however, this high point is of marginal statistical significance using our current pessimistic assessment of 95% confidence intervals.

Oxygen inventory changes between 1970 and 2010 are further assessed and compared against prior studies in Table 1. We find that the full ocean oxygen inventory decreased by $-0.84\% \pm 0.42\%$, with the near-surface (0–100 m) oxygen inventory reducing by $-0.85\% \pm 0.64\%$. These results are in line with prior studies included in the SROCC (Bindoff et al. 2022) assessment. In the naive case where ocean oxygen content was driven solely by temperature changes, we would expect changes in oxygen inventory and oxygen solubility to be identical. Examining global trends, we see that temperature-driven solubility changes explains 21% of the oxygen decline over the full water column. In the upper 100 m, solubility changes can explain all of the oxygen decrease, but for the 100–600 m depth range it can explain only 29%, reducing to 19% between 600 and 1000 m, and 11% in the deep ocean.

Figure 8 shows oxygen inventory anomalies as a function of latitude and time for the full depth of the ocean (Fig. 8a) and the SROCC depth ranges (Figs. 8b–e), and as a function of depth and time (Fig. 8f). While the full depth (Fig. 8a), upper

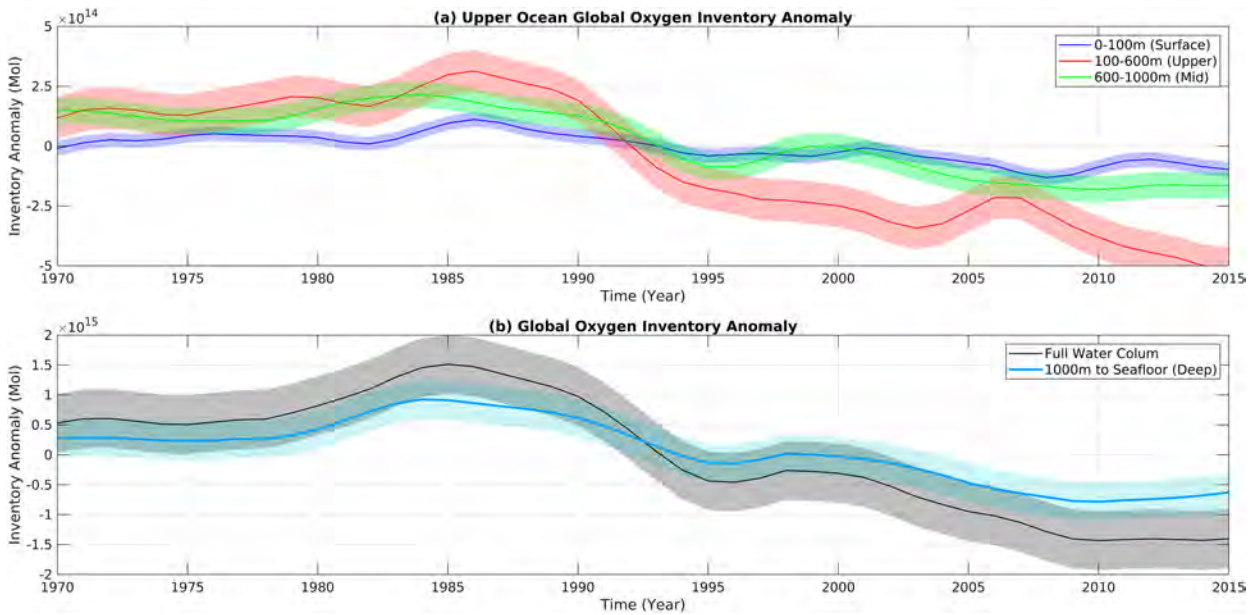


FIG. 7. Oxygen anomaly inventories and 95% confidence intervals for (a) the surface ocean (dark blue), upper ocean (red), and middepth ocean (green) and (b) the deep ocean (light blue) and full water column (black).

ocean (Fig. 8c), midocean (Fig. 8d), and deep ocean (Fig. 8e) inventories show statistically significant declines between 1970 and 2000–15 (at the 2σ level) across most latitudes the surface ocean (Fig. 8b) does not. However, in addition to the long-term decline we also see significant decadal-scale variability with an increase in oxygen inventory starting in the Southern Hemisphere in the late 1960s and moving into the Northern Hemisphere in the early to mid-1970s in the upper and midocean, and the late 1970s in the deep ocean, before global oxygen decline comes to dominate in the late 1980s and onward. The depth inventories (Fig. 8f) suggests this interdecadal oxygen increase commences in the upper ocean in the early to mid-1960s before spreading into the deep ocean in the late 1970s; this high oxygen subsequently is eroded starting in the surface layer in the upper ocean in the mid-1980s and extending into the deep ocean in the late 1980s to mid-1990s.

Maps of percentage change in oxygen inventory and oxygen solubility “inventory” between 1970 and 2010 are shown in Fig. 9. We observe that changes in oxygen concentration are typically larger than can be explained by solubility alone and that the spatial distribution of oxygen inventory and saturation changes are frequently anticorrelated.

The surface ocean (0–100 m, Fig. 9a) shows increases in oxygen concentration over the North Atlantic and much of the Pacific. In the North Atlantic we see the strongest increases in the Gulf Stream and along the eastern coast of Greenland, while in the Pacific we see increasing oxygen along the equator and gyre rims, with declining oxygen in the gyre interiors, along the North American coast, and in the Kuroshio. The southern Indian Ocean and Southern Ocean predominately show neutral to weak decreases in oxygen inventory. Marginal seas display a variety of behaviors; the Mediterranean, Gulf of Mexico, South China Sea, Arabian Sea, Coral Sea, and Sea of Okhotsk show increases in oxygen content, while the Bay of Bengal, Sea of Japan, and East China Sea show clear declines. The Caribbean Sea and Tasman Sea show no significant changes.

The pattern of increases in surface oxygen saturation are not explained by the reduced saturation estimated from the warming of these regions (Fig. 9b). However, there is some evidence that biological activity can cause supersaturation of the surfaces associated with increased oxygen production from “greening” of the ocean in some Earth system models (Henson et al. 2010) and from remotely sensed observations of chlorophyll (Gregg and Rousseaux 2019). The pattern of

TABLE 1. Percentage change in oxygen inventories assessed from this study and earlier results as synthesized from the SROCC chapter 5 (Bindoff et al. 2022), Table 5.2 (p. 472). Error bars for prior studies and SROCC assessment are 90% confidence intervals, and error bars for this study are 95% confidence intervals.

	Helm et al. (2011)	Ito et al. (2017)	Schmidtke et al. (2017)	SROCC	This study
Full depth	-0.87 ± 0.53	—	-1.43 ± 0.70	-1.15 ± 0.88	-0.84 ± 0.42
0–100 m	-1.30 ± 0.54	-1.65 ± 0.63	-0.38 ± 1.06	-1.11 ± 0.95	-0.85 ± 0.64
100–600 m	-2.04 ± 0.60	-3.17 ± 1.34	-1.06 ± 1.36	-2.09 ± 1.42	-1.72 ± 0.80
600 m–seafloor	-0.81 ± 0.57	—	-1.51 ± 0.62	-1.16 ± 0.84	-0.71 ± 0.47

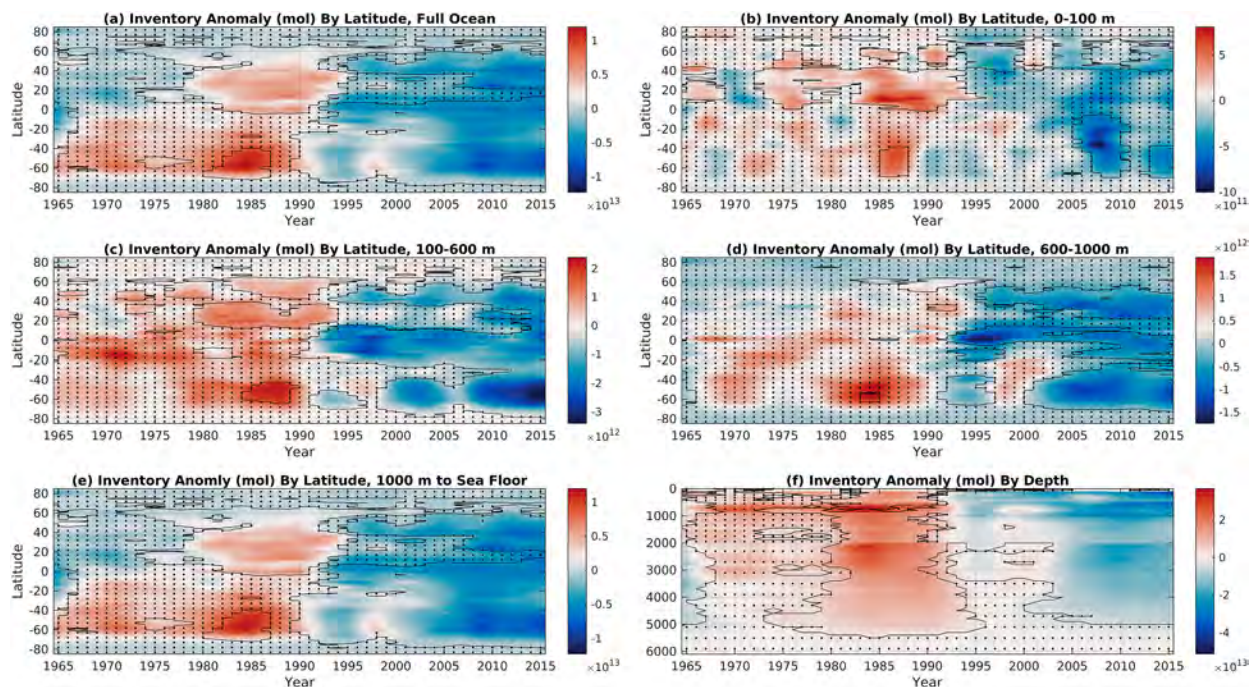


FIG. 8. Oxygen inventory anomalies as a function of time and latitude for (a)–(e) selected depth ranges and (f) depth. Dotted areas indicate where the change in oxygen inventory is not significant at the 2σ level relative to the 1970 value.

saturation change in these ocean basins largely coincides with the pattern of primary productivity increases (Bindoff et al. 2022; Gregg and Rousseaux 2019).

The upper ocean (100–600 m, Figs. 9c,d) demonstrates strong decreases in oxygen inventory associated with expansion of the oxygen minimum zones in the east Pacific, equatorial Atlantic, and the Indian Ocean, and in the Southern Ocean likely relating to increased upwelling of low oxygen deep waters driven by increasing wind speed (Waugh et al. 2013). We see increases in oxygen in the North Atlantic, tropical western North Pacific, the central South Pacific, and the Tasman Sea in a pattern consistent with the residual downwelling seen in Liang et al. (2017), suggesting these upward trends may be driven by increased downwelling of oxygen rich surface waters. As above changes in oxygen saturation do not explain the changes observed in oxygen inventory.

In the midocean and deep ocean (600–1000 m, Fig. 9e, and 1000 m to the seafloor, Fig. 9g) oxygen change is dominated by large decreases in the Southern Ocean, moderate decreases in the Pacific and South Atlantic Oceans, and minor decreases to small increases in the Indian and North Atlantic Oceans. These changes in oxygen content are too large to be explained by solubility (Figs. 9f,h), but are consistent with our present understanding of changes to the lower limb of the global overturning circulation, which includes a slowing of deep ocean ventilation (Purkey et al. 2019; Bindoff et al. 2022).

5. Conclusions

We have created a new atlas of oxygen, salinity, and temperature using Data Interpolating Variational Analysis (Troupin

et al. 2012; Barth et al. 2014). This atlas has a spatial grid of $1/2^\circ \times 1/2^\circ$, which represents an improvement over prior oxygen atlases (e.g., Schmidtko et al. 2017; Ito et al. 2017; Ito 2022). The use of DIVAnd combined with CMCC Historical Ocean Reanalysis (CHOR) velocity fields means that our atlas is tied to tracer advection and coastal boundary conditions. Consequently, this approach explicitly removes leakage of artificial signals across topographic barriers, driving a more “tracer-like” behavior of the interpolated variables. This approach is a natural and physically consistent inclusion and overcomes the ad hoc approaches of treating topography and coastlines in earlier atlases using optimal interpolation (e.g., Bretherton et al. 1976). It is a straightforward process to update to the present when additional profile data become progressively available and to add further variables like nitrate and phosphate. This atlas is suitable for detection and attribution studies of human influence on oxygen decline and vastly improves the atlases used in earlier studies (e.g., Andrews et al. 2013; Helm et al. 2011).

Our atlas shows good agreement in structure with the present understanding of oxygen distribution in the world’s oceans. We find a decrease in global oxygen full-depth inventory of $-0.84\% \pm 0.42\%$ change over the period 1970–2010, the upper ocean (0–100 m) shows a change of $-0.85\% \pm 0.64\%$, while the midocean (100–600 m) and deep ocean (600 m and deeper) show changes of $-1.72\% \pm 0.80\%$ and $-0.71\% \pm 0.47\%$, respectively. These estimates are comparable with prior studies and the IPCC SROCC assessment (Bindoff et al. 2022). We find that temperature-driven solubility changes explain 29% of the oxygen inventory change in the upper ocean, reducing to 11%

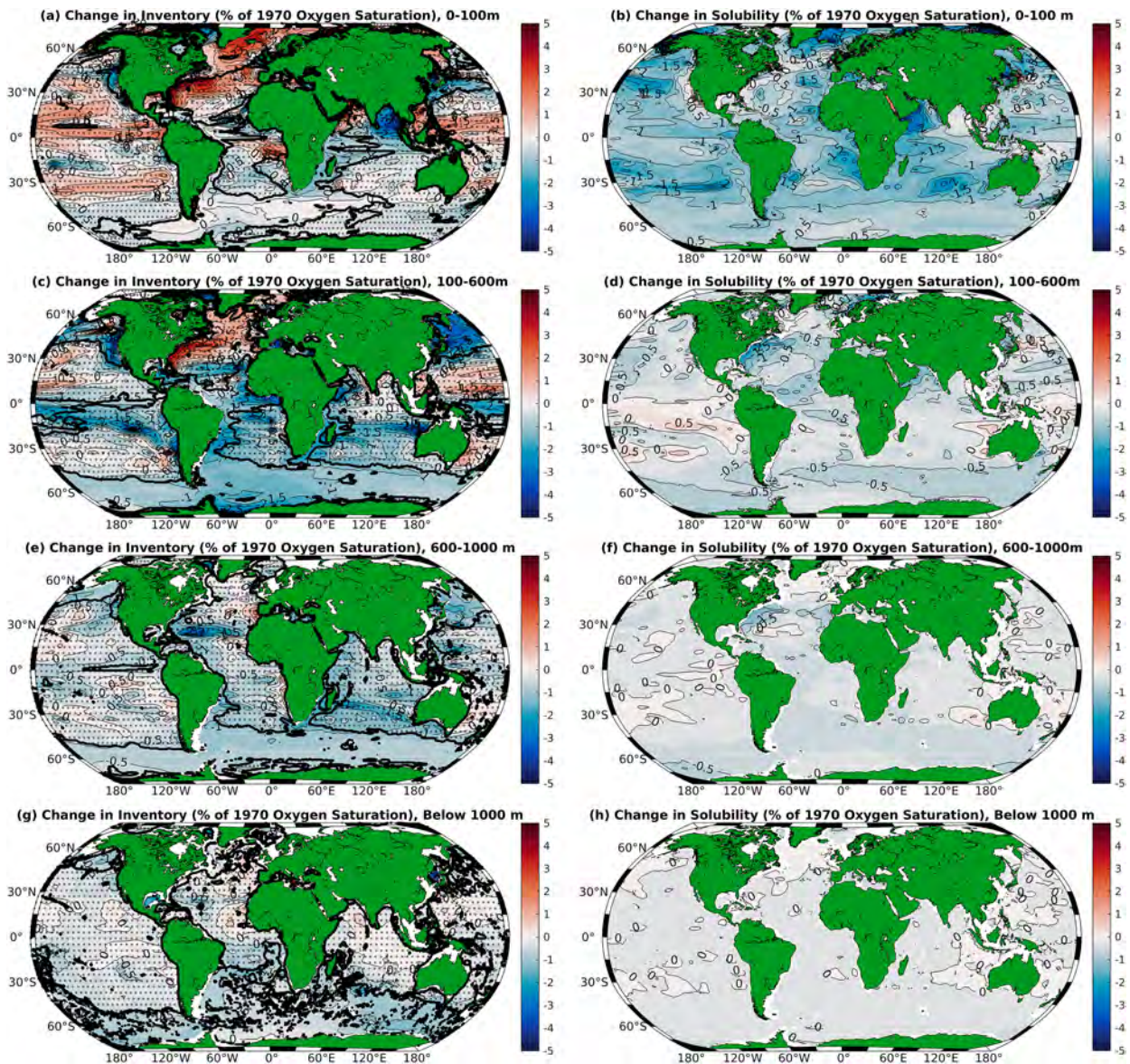


FIG. 9. Maps of changes in (a),(c),(e),(g) oxygen inventories and (b),(d),(f),(g) oxygen solubility from 1970 to 2010 for (a),(b) the surface layer, (c),(d) 100–600 m, (e),(f) 600–1000 m, and (g),(h) below 1000 m. Dotted areas indicate where the change in oxygen inventory is not significant at the 2σ level relative to the 1970 value.

in the deep ocean. These results mean that a substantial fraction of the oxygen declines observed in the oceans are driven by physical changes in the ocean, such as increased stratification (Bindoff et al. 2022), reduced subduction, or by biological activity through a slower circulation and increased oxygen consumption (Bindoff and McDougall 2000).

Examining changes on a regional basis in the surface ocean (0–100 m), we see some significant areas of increasing oxygen inventory, potentially explained by “greening” of the upper ocean causing enhanced oxygen production (Henson et al. 2010; Bindoff et al. 2022). The upper ocean is dominated by decreases in oxygen and expansion of the oxygen minimum

zones likely driven by upwelling of deep waters driven by increased wind (Vaugh et al. 2013). The mid- and deep ocean are dominated by decreased oxygen in the South Atlantic, Pacific, and Southern Oceans, consistent with a slowing of deep ocean ventilation (e.g., Purkey et al. 2019).

Potential future work includes using the atlas for detection and attribution analysis; extending the mapping to other biogeochemical parameters; refining the error analysis and updating the atlas to include data from biogeochemical Argo floats, validation of biogeochemical simulations, and examining the temporal changes in more detail. For example, there is an increase in oxygen seen in the deep Southern Ocean in the

early part of the time series (from 1970s and peaking in 1985, Fig. 7).

Acknowledgments. We wish to thank two anonymous reviewers who provided useful guidance on improving the presentation of this paper. This work was undertaken during Christopher Roach's time at the University of Tasmania, LOCEAN-IPSL, and MetOcean Solutions (a division of Meteorological Service of New Zealand). We wish to acknowledge the support provided by all three institutions in time and compute resources. This study uses data from NOAA's World Ocean Database 2018 and the DIVAnd software produced by GHER at the University of Liege. This project received grant funding from the Australian Government as part of the National Environmental Science Program (NESP) and the Antarctic Science Collaboration Initiative program (ASCI000002). This research was supported by the Australian Research Council Special Research Initiative, Australian Centre for Excellence in Antarctic Science (Project SR200100008).

Data availability statement. World Ocean Database 2018 temperature, salinity, and oxygen data are available from <https://www.nci.noaa.gov/products/world-ocean-database>. The CMCC Historical Ocean Reanalysis is available from <http://c-glors.cmcc.it/index/index-3.html?sec=2>. The oxygen, temperature, and salinity atlases (including error fields) produced during this study are available from the IMAS Data Portal (<https://metadata.imas.utas.edu.au/geonetwork/srv/eng/catalog.search#/metadata/aef9f21a-c60f-46c0-84a0-76fe541180fa>). Auxiliary data are available on request.

APPENDIX

Supplementary Figures

Figures A1 and A2 present example background oxygen concentration maps and example correlation maps for DIVAnd over a range of different correlation scales and advection weighting. Details are discussed in section 3c.

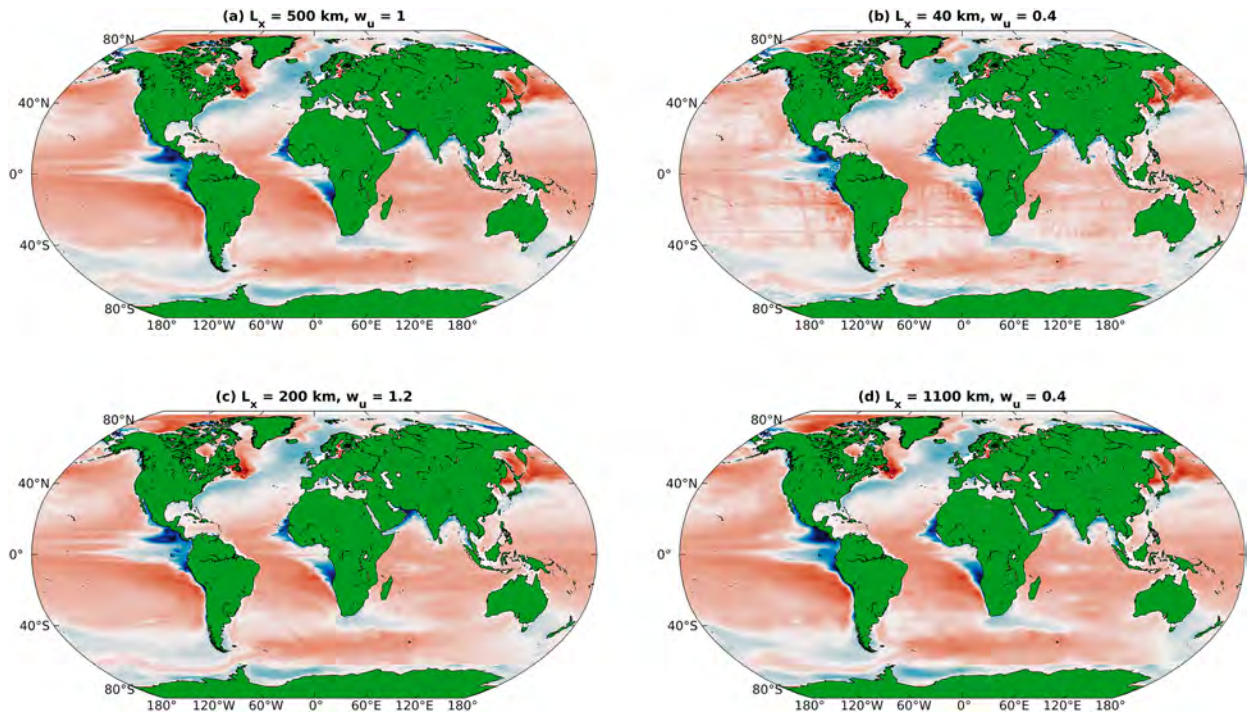


FIG. A1. Example background oxygen concentration ($\mu\text{mol kg}^{-1}$) maps for a range of different L_x and w_u .

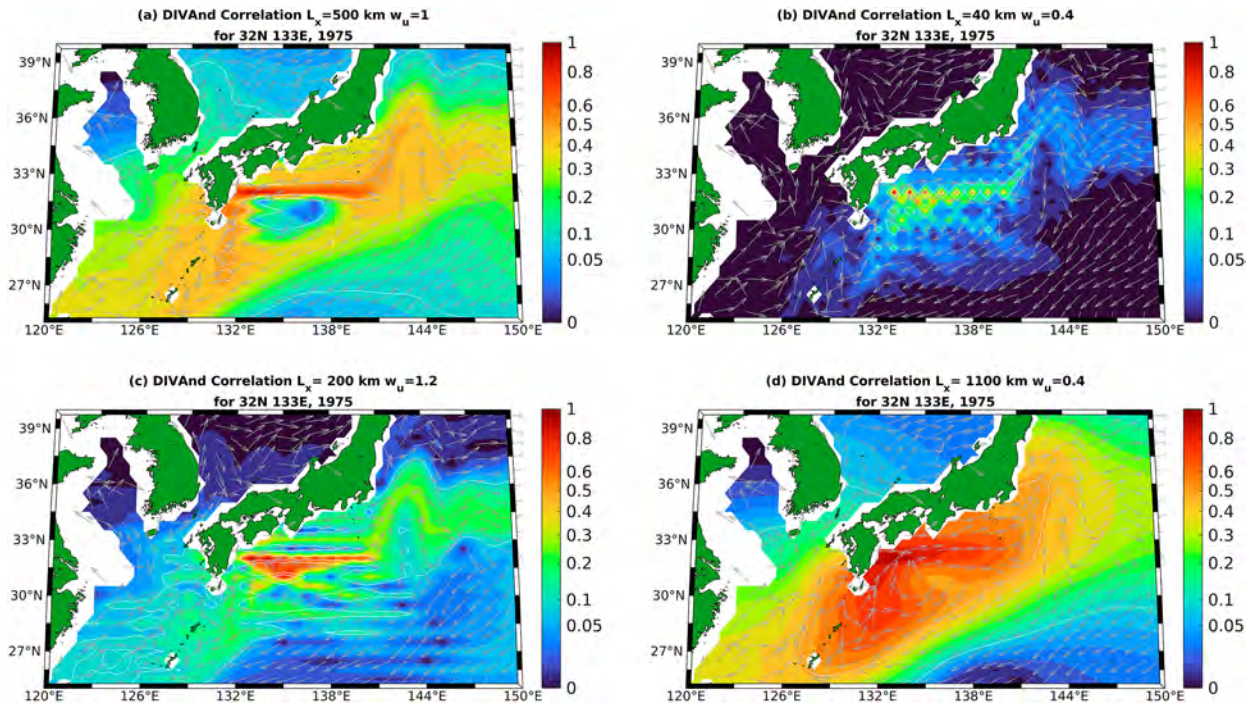


FIG. A2. Example correlation maps (1975; 50 m depth) for DIVAnd relative to 32°N, 133°E in the Kuroshio region for a range of different L_x and w_u .

REFERENCES

- Andrews, O. D., N. L. Bindoff, P. R. Halloran, T. Ilyina, and C. Le Quéré, 2013: Detecting an external influence on recent changes in oceanic oxygen using an optimal fingerprinting method. *Biogeosciences*, **10**, 1799–1813, <https://doi.org/10.5194/bg-10-1799-2013>.
- Barth, A., J.-M. Beckers, C. Troupin, A. Alvera-Azcárate, and L. Vandenbulcke, 2014: divand-1.0: n -dimensional variational data analysis for ocean observations. *Geosci. Model Dev.*, **7**, 225–241, <https://doi.org/10.5194/gmd-7-225-2014>.
- Belgacem, M., and Coauthors, 2021: Climatological distribution of dissolved inorganic nutrients in the western Mediterranean Sea (1981–2017). *Earth Syst. Sci. Data*, **13**, 5915–5949, <https://doi.org/10.5194/essd-13-5915-2021>.
- Bindoff, N. L., and C. Wunsch, 1992: Comparison of synoptic and climatologically mapped sections in the South Pacific Ocean. *J. Climate*, **5**, 631–645, [https://doi.org/10.1175/1520-0442\(1992\)005<0631:COACM>2.0.CO;2](https://doi.org/10.1175/1520-0442(1992)005<0631:COACM>2.0.CO;2).
- , and T. J. McDougall, 2000: Decadal changes along an Indian Ocean section at 32°S and their interpretation. *J. Phys. Oceanogr.*, **30**, 1207–1222, [https://doi.org/10.1175/1520-0485\(2000\)030<1207:DCAAO>2.0.CO;2](https://doi.org/10.1175/1520-0485(2000)030<1207:DCAAO>2.0.CO;2).
- , and Coauthors, 2022: Changing ocean, marine ecosystems, and dependent communities. *The Ocean and Cryosphere in a Changing Climate*, Cambridge University Press, 447–588, <https://doi.org/10.1017/9781009157964.007>.
- Bittig, H. C., and A. Körtzinger, 2015: Tackling oxygen optode drift: Near-surface and in-air oxygen optode measurements on a float provide an accurate in situ reference. *J. Atmos. Oceanic Technol.*, **32**, 1536–1543, <https://doi.org/10.1175/JTECH-D-14-00162.1>.
- Bograd, S. J., and Coauthors, 2015: Changes in source waters to the Southern California Bight. *Deep-Sea Res. II*, **112**, 42–52, <https://doi.org/10.1016/j.dsr2.2014.04.009>.
- Boyer, T. P., and Coauthors, 2018: World Ocean Database 2018. NOAA Atlas NESDIS 87, 207 pp., https://www.ncei.noaa.gov/sites/default/files/2020-04/wod_intro_0.pdf.
- Bretherton, F. P., R. E. Davis, and C. Fandry, 1976: A technique for objective analysis and design of oceanographic experiments applied to MODE-73. *Deep Sea Res. Oceanogr. Abstr.*, **23**, 559–582, [https://doi.org/10.1016/0011-7471\(76\)90001-2](https://doi.org/10.1016/0011-7471(76)90001-2).
- Buchanan, P. J., R. J. Matear, Z. Chase, S. J. Phipps, and N. L. Bindoff, 2018: Dynamic biological functioning important for simulating and stabilizing ocean biogeochemistry. *Global Biogeochem. Cycles*, **32**, 565–593, <https://doi.org/10.1002/2017GB005753>.
- Bushinsky, S. M., S. R. Emerson, S. C. Riser, and D. D. Swift, 2016: Accurate oxygen measurements on modified Argo floats using in situ air calibrations. *Limnol. Oceanogr. Methods*, **14**, 491–505, <https://doi.org/10.1002/lom3.10107>.
- Capet, A., C. Troupin, J. Carstensen, M. Grégoire, and J.-M. Beckers, 2014: Untangling spatial and temporal trends in the variability of the Black Sea cold intermediate layer and mixed layer depth using the DIVA detrending procedure. *Ocean Dyn.*, **64**, 315–324, <https://doi.org/10.1007/s10236-013-0683-4>.
- Carton, J. A., and B. S. Giese, 2008: A reanalysis of ocean climate using Simple Ocean Data Assimilation (SODA). *Mon. Wea. Rev.*, **136**, 2999–3017, <https://doi.org/10.1175/2007MWR1978.1>.

- Chen, Y., T. A. Davis, W. W. Hager, and S. Rajamanickam, 2008: Algorithm 887: CHOLMOD, supernodal sparse Cholesky factorization and update/downdate. *ACM Trans. Math. Software*, **35**, 22, <https://doi.org/10.1145/1391989.1391995>.
- Claustre, H., K. S. Johnson, and Y. Takeshita, 2020: Observing the global ocean with Biogeochemical-Argo. *Annu. Rev. Mar. Sci.*, **12**, 23–48, <https://doi.org/10.1146/annurev-marine-010419-010956>.
- Compo, G. P., J. S. Whitaker, and P. D. Sardeshmukh, 2006: Feasibility of a 100-year reanalysis using only surface pressure data. *Bull. Amer. Meteor. Soc.*, **87**, 175–190, <https://doi.org/10.1175/BAMS-87-2-175>.
- Culberson, C. H., 1991: Dissolved oxygen. WHP Operations and Methods Doc., 15 pp., https://cchdo.github.io/hdo-assets/documentation/manuals/pdf/91_1/culber2.pdf.
- Davis, T. A., and W. W. Hager, 2009: Dynamic supernodes in sparse Cholesky update/downdate and triangular solves. *ACM Trans. Math. Software*, **35**, 27, <https://doi.org/10.1145/1462173.1462176>.
- Dickson, A. G., 1994: Determination of dissolved oxygen in sea water by Winkler titration. WHP Operations and Methods Doc., 13 pp., https://cchdo.github.io/hdo-assets/documentation/manuals/pdf/91_1/dickson2.pdf.
- Dogliani, F., R. Ricker, B. Rabe, A. Barth, C. Troupin, and T. Kanzow, 2023: Sea surface height anomaly and geostrophic current velocity from altimetry measurements over the Arctic Ocean (2011–2020). *Earth Syst. Sci. Data*, **15**, 225–263, <https://doi.org/10.5194/essd-15-225-2023>.
- Ducet, N., P. Y. Le Traon, and G. Reverdin, 2000: Global high-resolution mapping of ocean circulation from TOPEX/Poseidon and ERS-1 and -2. *J. Geophys. Res.*, **105**, 19 477–19 498, <https://doi.org/10.1029/2000JC900063>.
- Fukumori, I., P. Heimbach, R. M. Ponte, and C. Wunsch, 2018: A dynamically consistent, multivariable ocean climatology. *Bull. Amer. Meteor. Soc.*, **99**, 2107–2128, <https://doi.org/10.1175/BAMS-D-17-0213.1>.
- Gamo, T., and Y. Horibe, 1980: Precise determination of dissolved gases in sea water by shipboard gas chromatography. *Bull. Chem. Soc. Japan*, **53**, 2839–2842, <https://doi.org/10.1246/bcsj.53.2839>.
- Garcia, H. E., T. P. Boyer, O. K. B. Ricardo A. Locarnini, and M. M. Zweng, 2018: World Ocean Database 2018: User's manual (pre-release). NOAA Atlas NESDIS 83, 111 pp., <https://www.ncei.noaa.gov/sites/default/files/2020-04/wodreadme.pdf>.
- Gregg, W. W., and C. S. Rousseaux, 2019: Global ocean primary production trends in the modern ocean color satellite record (1998–2015). *Environ. Res. Lett.*, **14**, 124011, <https://doi.org/10.1088/1748-9326/ab4667>.
- Helm, K. P., N. L. Bindoff, and J. A. Church, 2011: Observed decreases in oxygen content of the global ocean. *Geophys. Res. Lett.*, **38**, L23602, <https://doi.org/10.1029/2011GL049513>.
- Henson, S. A., J. L. Sarmiento, J. P. Dunne, L. Bopp, I. Lima, S. C. Doney, J. John, and C. Beaulieu, 2010: Detection of anthropogenic climate change in satellite records of ocean chlorophyll and productivity. *Biogeosciences*, **7**, 621–640, <https://doi.org/10.5194/bg-7-621-2010>.
- Ito, T., 2022: Optimal interpolation of global dissolved oxygen: 1965–2015. *Geosci. Data J.*, **9**, 167–176, <https://doi.org/10.1002/gdj3.130>.
- , S. Minobe, M. C. Long, and C. Deutsch, 2017: Upper ocean O₂ trends: 1958–2015. *Geophys. Res. Lett.*, **44**, 4214–4223, <https://doi.org/10.1002/2017GL073613>.
- Janson, L., W. Fithian, and T. J. Hastie, 2015: Effective degrees of freedom: A flawed metaphor. *Biometrika*, **102**, 479–485, <https://doi.org/10.1093/biomet/asv019>.
- Langdon, C., 2010: Determination of dissolved oxygen in seawater by Winkler titration using the amperometric technique. The GO-SHIP repeat hydrography manual: A collection of expert reports and guidelines, IOCCP Rep. 14, 18 pp., https://www.go-ship.org/Manual/Langdon_Amperometric_oxygen.pdf.
- Levitus, S., 1983: Climatological atlas of the world ocean. *Eos, Trans. Amer. Geophys. Union*, **64**, 962–963, <https://doi.org/10.1029/EO064i049p00962-02>.
- Liang, X., M. Spall, and C. Wunsch, 2017: Global ocean vertical velocity from a dynamically consistent ocean state estimate. *J. Geophys. Res. Oceans*, **122**, 8208–8224, <https://doi.org/10.1002/2017JC012985>.
- Lozier, M. S., M. S. McCartney, and W. B. Owens, 1994: Anomalous anomalies in averaged hydrographic data. *J. Phys. Oceanogr.*, **24**, 2624–2638, [https://doi.org/10.1175/1520-0485\(1994\)024<2624:AAIAHD>2.0.CO;2](https://doi.org/10.1175/1520-0485(1994)024<2624:AAIAHD>2.0.CO;2).
- Luyten, J. R., M. Fieux, and J. Gonella, 1980: Equatorial currents in the western Indian Ocean. *Science*, **209**, 600–603, <https://doi.org/10.1126/science.209.4456.600>.
- McDougall, T. J., and P. M. Barker, 2011: Getting started with TEOS-10 and the Gibbs Seawater (GSW) oceanographic toolbox. SCOR/IAPSO WG127 Doc., 34 pp., https://www.teos-10.org/pubs/Getting_Started.pdf.
- Montgomery, H., N. Thom, and A. Cockburn, 1964: Determination of dissolved oxygen by the Winkler method and the solubility of oxygen in pure water and sea water. *J. Appl. Chem.*, **14**, 280–296, <https://doi.org/10.1002/jctb.5010140704>.
- Oschlies, A., P. Brandt, L. Stramma, and S. Schmidtko, 2018: Drivers and mechanisms of ocean deoxygenation. *Nat. Geosci.*, **11**, 467–473, <https://doi.org/10.1038/s41561-018-0152-2>.
- Purkey, S. G., G. C. Johnson, L. D. Talley, B. M. Sloyan, S. E. Wijffels, W. Smethie, S. Mecking, and K. Katsumata, 2019: Unabated bottom water warming and freshening in the South Pacific Ocean. *J. Geophys. Res. Oceans*, **124**, 1778–1794, <https://doi.org/10.1029/2018JC014775>.
- Rayner, N. A., D. E. Parker, E. B. Horton, C. K. Folland, L. V. Alexander, D. P. Rowell, E. C. Kent, and A. Kaplan, 2003: Global analyses of sea surface temperature, sea ice, and night marine air temperature since the late nineteenth century. *J. Geophys. Res.*, **108**, 4407, <https://doi.org/10.1029/2002JD002670>.
- Ridgway, K. R., J. R. Dunn, and J. L. Wilkin, 2002: Ocean interpolation by four-dimensional weighted least squares—Application to the waters around Australasia. *J. Atmos. Oceanic Technol.*, **19**, 1357–1375, [https://doi.org/10.1175/1520-0426\(2002\)019<1357:OIBFDW>2.0.CO;2](https://doi.org/10.1175/1520-0426(2002)019<1357:OIBFDW>2.0.CO;2).
- Riser, S. C., D. Swift, and R. Drucker, 2018: Profiling floats in SOCCOM: Technical capabilities for studying the Southern Ocean. *J. Geophys. Res. Oceans*, **123**, 4055–4073, <https://doi.org/10.1002/2017JC013419>.
- Roach, C. J., and N. L. Bindoff, 2023: Roach and Bindoff global temperature, salinity and oxygen atlas (shipboard data 1955–2018) v1.0. IMAS, <https://doi.org/10.25959/hk4q-b239>.
- Sasano, D., Y. Takatani, N. Kosugi, T. Nakano, T. Midorikawa, and M. Ishii, 2015: Multidecadal trends of oxygen and their controlling factors in the western North Pacific. *Global Biogeochem. Cycles*, **29**, 935–956, <https://doi.org/10.1002/2014GB005065>.
- Schmidtko, S., L. Stramma, and M. Visbeck, 2017: Decline in global oceanic oxygen content during the past five decades. *Nature*, **542**, 335–339, <https://doi.org/10.1038/nature21399>.

- Storto, A., S. Dobricic, S. Masina, and P. D. Pietro, 2011: Assimilating along-track altimetric observations through local hydrostatic adjustment in a global ocean variational assimilation system. *Mon. Wea. Rev.*, **139**, 738–754, <https://doi.org/10.1175/2010MWR3350.1>.
- Talley, L., and Coauthors, 2016: Changes in ocean heat, carbon content, and ventilation: A review of the first decade of GO-SHIP global repeat hydrography. *Annu. Rev. Mar. Sci.*, **8**, 185–215, <https://doi.org/10.1146/annurev-marine-052915-100829>.
- Tchebichef, P., 1867: Des valeurs moyennes. *J. Math. Pures Appl.*, **12**, 177–184.
- Tellinghuisen, J., 2001: Statistical error propagation. *J. Phys. Chem.*, **105A**, 3917–3921, <https://doi.org/10.1021/jp003484u>.
- Terada, M., and S. Minobe, 2018: Projected sea level rise, gyre circulation and water mass formation in the western North Pacific: CMIP5 inter-model analysis. *Climate Dyn.*, **50**, 4767–4782, <https://doi.org/10.1007/s00382-017-3902-8>.
- Troupin, C., F. Machín, M. Ouberdous, D. Sirjacobs, A. Barth, and J.-M. Beckers, 2010: High-resolution climatology of the northeast Atlantic using Data-Interpolating Variational Analysis (DIVA). *J. Geophys. Res.*, **115**, C08005, <https://doi.org/10.1029/2009JC005512>.
- , and Coauthors, 2012: Generation of analysis and consistent error fields using the Data Interpolating Variational Analysis (DIVA). *Ocean Modell.*, **52–53**, 90–101, <https://doi.org/10.1016/j.ocemod.2012.05.002>.
- , M. Ouberdous, D. Sirjacobs, A. Alvera-Azcárate, A. Barth, M.-E. Toussaint, S. Watelet, and J.-M. Beckers, 2017: gherul/Diva-User-Guide: v1.0. Zenodo, <https://doi.org/10.5281/zenodo.836723>.
- Verdy, A., and M. R. Mazloff, 2017: A data assimilating model for estimating Southern Ocean biogeochemistry. *J. Geophys. Res. Oceans*, **122**, 6968–6988, <https://doi.org/10.1002/2016JC012650>.
- Waugh, D. W., F. Primeau, T. DeVries, and M. Holzer, 2013: Recent changes in the ventilation of the Southern Oceans. *Science*, **339**, 568–570, <https://doi.org/10.1126/science.1225411>.
- Whitney, F. A., H. J. Freeland, and M. Robert, 2007: Persistently declining oxygen levels in the interior waters of the eastern subarctic Pacific. *Prog. Oceanogr.*, **75**, 179–199, <https://doi.org/10.1016/j.pocean.2007.08.007>.
- Wong, A. P. S., N. L. Bindoff, and J. A. Church, 2001: Freshwater and heat changes in the North and South Pacific Oceans between the 1960s and 1985–94. *J. Climate*, **14**, 1613–1633, [https://doi.org/10.1175/1520-0442\(2001\)014<1613:FAHCIT>2.0.CO;2](https://doi.org/10.1175/1520-0442(2001)014<1613:FAHCIT>2.0.CO;2).
- Wunsch, C., 1996: *The Ocean Circulation Inverse Problem*. Cambridge University Press, 442 pp.
- , P. Heimbach, R. M. Ponte, and I. Fukumori, 2009: The global general circulation of the ocean estimated by the ECCO-Consortium. *Oceanography*, **22** (2), 88–103, <https://doi.org/10.5670/oceanog.2009.41>.
- Wüst, G., 1936: Deep circulation in the expanse of the North Atlantic Ocean. *Int. Hydrogr. Rev.*, **13**, 23–31.
- Yang, C., S. Masina, and A. Storto, 2017: Historical ocean reanalyses (1900–2010) using different data assimilation strategies. *Quart. J. Roy. Meteor. Soc.*, **143**, 479–493, <https://doi.org/10.1002/qj.2936>.